Available online at www.sciencedirect.com
ScienceDirect
Journal of Computational Physics 227 (2008) 3260–3281
JOURNAL OF COMPUTATIONAL PHYSICS
www.elsevier.com/locate/jcp

A guiding centre direct implicit scheme for magnetized plasma simulations

F. Mottez *

LUTH, Observatoire de Paris, CNRS, Université Paris Diderot; 5 Place Jules Janssen, 92190 Meudon, France

Received 13 February 2007; received in revised form 19 November 2007; accepted 25 November 2007
Available online 8 December 2007

Abstract

A new implicit fully electromagnetic particle in cell method is presented in which the full ion dynamic and all the electron guiding centre drifts of a magnetized collisionless plasma are retained. This code retains the inertial effects on the electrons. It must be used for time steps larger or so than an electron cyclotron period, it is only valid for an electron plasma beta $\beta_e < 1$. Therefore, it is efficient only with strongly magnetized electrons. On the opposite, the constraint on the ions $\beta_i < m_i/m_e$ (where m_i/m_e is the ion to electron mass ratio) is very weak. This method allows for the simulation of an ion-beam instability (triggering electrostatic ion cyclotron waves and filamentation of the plasma), the propagation of MHD waves, and ion-temperature anisotropies (mirror and/or cyclotron waves), at a relatively low cost. This method could become a useful tool for the modelization of space plasmas, quite complementary with other methods such as Hall-MHD, hybrid codes, or other implicit particle codes.

PACS: 52.65.−y; 52.65.Rr; 52.25.Xz; 52.35.−g; 52.35.Bj

Keywords: Plasma: numerical simulation; Implicit algorithm; Particles in cell; Electron guiding centre

1. Introduction

When simulating an electromagnetic plasma with an explicit particle in cell (PIC) code, several time scales must be taken into account. The aim of an implicit code is to solve the equations of evolution of a dynamical system without keeping the high frequency fluctuations. For instance time decentered schemes are made implicit by the time-discretization method, in which the intermediate time level is slightly decentered [1–6]. In the direct implicit scheme, a few variables of the system (at time step n) are replaced by time averaged implicit variables. These implicit variables depend both on the state of the system in the past (time $n-1$) and in the future (time $n+1$) [7,8].

Our purpose is to develop an integration scheme for particle in cell (PIC) algorithm, that allows the description of the ion full dynamics and the electron guiding centre dynamics, based on the direct implicit algorithm,

* Tel.: +33 1 45077773.
E-mail address: fabrice.mottez@obspm.fr

0021-9991/$ - see front matter © 2007 Elsevier Inc. All rights reserved.
doi:10.1016/j.jcp.2007.11.034

accurate to the second order in Δt. We aim to get rid of the constraints imposed by the light waves (propagating at the velocity c and not interfering with the plasma), the electron gyromotion (at frequency ω_{ce}), and the plasma oscillations (at frequency ω_{pe}), and in case of implicitness over the ion motion, the ion plasma oscillations (at frequency ω_{pi}).

We need to solve the Maxwell's equations

$$\nabla \times \mathbf{E} = -\frac{\partial \mathbf{B}}{\partial t}, \tag{1}$$

$$\nabla \times \mathbf{H} = \mathbf{J} + \frac{\partial \mathbf{D}}{\partial t}, \tag{2}$$

$$\nabla \cdot \mathbf{D} = \rho, \tag{3}$$

$$\nabla \cdot \mathbf{B} = 0. \tag{4}$$

The Maxwell equations are coupled to the particle dynamical data through the definition of the charge ρ and the electric current $\mathbf{J}$ densities. The ion equation of motion is

$$m\frac{\mathrm{d}\mathbf{v}}{\mathrm{d}t} = e(\mathbf{E} + \mathbf{v} \times \mathbf{B}). \tag{5}$$

To the first order in m/e, the instantaneous acceleration $\mathrm{d}\mathbf{v}/\mathrm{d}t$ of the guiding centre position $\mathbf{r}$ is given [9] by

$$m\frac{\mathrm{d}\mathbf{v}}{\mathrm{d}t} = -e[\mathbf{E}(\mathbf{r}) + \mathbf{v} \times \mathbf{B}(\mathbf{r})] - \mu \nabla B(\mathbf{r}), \tag{6}$$

where B is the modulus of the magnetic field $\mathbf{B}$. The basic Eq. (6) is similar to the particle equation of motion, provided that we use $\mathbf{E}(\mathbf{r}) + (\mu/e)\nabla \mathbf{B}(\mathbf{r})$ instead of $\mathbf{E}(\mathbf{r})$. Note that Eq. (6) contains all the drift terms, including the magnetic field gradient, the magnetic field line curvature and the polarization drifts. But this equation gives a solution whose instantaneous value is not physically relevant, only the low frequency part of the solution has a physical meaning (the guiding centre drifts). Therefore, it can be solved with a time step $\Delta t \omega_{ce} > 1$, and the fast part of the solution must be eliminated. The removing of the high frequency part of the solution is done through and implicit definition of the transverse velocity. Eq. (6) has already been implemented in a PIC guiding centre code for the simulation of highly magnetized plasmas [10]. (This code was explicit upon the plasma fluctuations at the frequency ω_{pe}.)

We want a code applicable to highly magnetized plasmas ($\omega_{ce} \gg \omega_{pe}$) and more weakly magnetized plasmas ($0 < \omega_{ce} \ll \omega_{pe}$).

The scheme introduced in this paper is not the only PIC implicit algorithm.

Tanaka [1,2] developed an implicit PIC code, called HIDENEK, for collisionless plasmas. This code exists in two versions, one for the electron full dynamics, and one with electron guiding centres. We are, in this paper, concerned with the second version. It is based on time decentering implicit scheme, and it is first order accurate in time. The computation cycle is as follows: the particles are advanced at time step n, and the charge ρ^n and current densities J^n are derived from the particle positions and velocities. Then, the Maxwell's equations and the equation of evolution ($\rho^n \to \rho^{n+1}$) of the charge and current density evolution are coupled and solved, providing the electric field E^{n+1}, and closing a time step cycle. Let us notice that the guiding centre equations in HIDENEK are the classical drift equations that provide the time derivative of the parallel velocity and the instantaneous drifts in the perpendicular directions.

The moment method, implemented in the codes VENUS and CELESTE developed at the Los Alamos National Laboratory [3–6] is also based on time decentered discretized equations but the computational cycle is different. The charge and current densities are considered as the first moments of the particle distribution function and they can be advanced in time through the resolution of fluid-like equations: after the computation of the new particle velocities and positions, the charge ρ^n and current densities J^n at time step n are computed, as well as a few tensors that allows to find directly the values of ρ^{n+1} and current densities J^{n+1}. Then, the Maxwell equations are solved in a way that do not involve any coupling with the equation of motion of the particles.

A code developed by Hewett and Langdon [8] is based on the direct implicit algorithm and is second order accurate in time. In any direct implicit algorithm, the choice of the variables that are averaged determine what

kind of high frequency phenomena can be made implicit. Hewett and Langdon's code was designed to get rid of the constraints on the time step imposed by the light waves and by the electron (and sometimes the proton) plasma period. It was shown [10] that it is not well adapted to plasmas with a high magnetic field, because the constraint $\omega_{ce}\Delta t << 1$ must be filled. Nevertheless, Hewett and Langdon's work is an important reference used along the present paper. Many developments of the algorithm introduced here can be considered as extensions of the Hewtett and Langdon scheme to the case of magnetized plasmas to be simulated with a time step that is large in comparison of an electron cyclotron period.

The physical variables are reduced to dimensionless variables. Time and frequencies are normalized by the electron plasma frequency ω_{p0} that correspond to a reference background electron density n_0. Velocities are normalized to the speed of light c, and the magnetic field is given in terms of the dimensionless electron gyrofrequency ω_{ce}/ω_{p0}. The mass unit is the electron mass m_e. Therefore, the units (starting from the Maxwell Eq. in the MKSA system) are c/ω_{p0} for distances, ω_{p0}/c for wave vectors, e for charges, en_0 for the charge density, $c\omega_{ce}/\omega_{p0}$ for the electric field, and ce/ω_{p0} for the magnetic moment μ of the electrons. In the following parts of this paper, all the equations, numerical values and figures are expressed in this system of units.

The paper starts with a presentation of the implicit discretized equations and the way they are solved. The scheme has been implemented in a 2D code, and the results of a few tests are presented in Section 2. The conditions of use of this code are discussed in Section 3. A more general discussion and the conclusion are presented in Section 4.

2. Implicit discretized equations

2.1. The Maxwell's equations

The finite differenced Maxwell's equations are the same as in [8]. The Faraday equation is made implicit

$$\mathbf{B}_{n+1/2} - \mathbf{B}_{n-1/2} = -\Delta t \nabla \times \overline{\mathbf{E}}_{\mathbf{n}}. \tag{7}$$

The use of $\overline{\mathbf{E}}_{\mathbf{n}}$ allows for the time filtering of the light waves of frequency ω_l when $\omega_l \Delta t > 1$:

$$\overline{\mathbf{E}}_n = \frac{1}{2}[\mathbf{E}_{n+1} + \overline{\mathbf{E}}_{n-1}]. \tag{8}$$

The Ampere equation does not contain implicit terms. Therefore, the displacement current is fully retained. As it plays an important role in the electron inertial effect, it implies that the electron inertial length (or skin depth) c/ω_{pe} must be retained,

$$\mathbf{E}_{n+1} - \mathbf{E}_n = \Delta t \nabla \times \mathbf{B}_{n+1/2} - \Delta t \mathbf{J}_{n+1/2}. \tag{9}$$

As the magnetic field at time $n+1$ is needed in the particle pusher (this is also the case in explicit PIC codes), the following extrapolation is used but it is not a part of the Maxwell equations iteration process:

$$\mathbf{B}_{n+1} - \mathbf{B}_{n+1/2} = -\frac{1}{2}\Delta t \nabla \times \mathbf{E}_{n+1}. \tag{10}$$

2.2. The ion dynamics

The resolution of the ion full dynamic equations has been largely described in the literature, both for explicit [11,12] and implicit calculations [8]. In all cases,

$$\mathbf{x}_{n+1} = \mathbf{x}_n + \Delta t \mathbf{v}_{n+1/2}. \tag{11}$$

The computation of the velocity $\mathbf{v}_{n+1/2}$ depends on the time step.

For time steps $0.4\omega_{pi}^{-1} > \Delta t$, where $\omega_{pi} = (ne^2/\epsilon_0 m_i)^{1/2}$ is the ion plasma frequency, we can compute the ion velocity explicitly:

$$\mathbf{v}_{n+1/2} = \mathbf{v}_{n-1/2} + \Delta t\left[\frac{q}{m}\mathbf{E}_n + \frac{q}{2m}(\mathbf{v}_{n+1/2} + \mathbf{v}_{n-1/2}) \times \mathbf{B}_n(\mathbf{x}_n)\right], \tag{12}$$

where m is the reduced ion mass and q is the reduced electric charge ($q = +1$ for hydrogen ions). The ion velocity Eq. (12) is the same as in explicit codes and can be solved with the Boris algorithm [11].

For time steps $0.4\omega_{ci}^{-1} > \Delta t > 0.4\omega_{pi}^{-1}$, the ion dynamics must be treated implicitly. We adopt, the direct implicit approach described in [7,8].

$$\mathbf{v}_{n+1/2} = \mathbf{v}_{n-1/2} + \Delta t\left[\bar{\mathbf{a}}_n + \frac{q}{2m}(\mathbf{v}_{n+1/2} + \mathbf{v}_{n-1/2}) \times \mathbf{B}_n(\mathbf{x}_n)\right]. \tag{13}$$

The implicit ion acceleration is

$$\bar{\mathbf{a}}_n = \frac{1}{2}\left(\frac{q}{m}\mathbf{E}_{n+1} + \bar{\mathbf{a}}_{n-1}\right). \tag{14}$$

The velocity is cut into a prediction $\mathbf{v}_{n+1/2}$, and a correction $\tilde{\mathbf{v}}_{n+1/2}$. Following [7,8],

$$\tilde{\mathbf{v}}_{n+1/2} = \mathbf{v}_{n-1/2} + \frac{\Delta t}{2}\bar{\mathbf{a}}_{n-1} + \frac{q\Delta t}{2m}(\tilde{\mathbf{v}}_{n+1/2} + \mathbf{v}_{n-1/2}) \times \mathbf{B}_n(\mathbf{x}_n), \tag{15}$$

the other terms are contained in the correction:

$$\delta\mathbf{v}_{n+1/2} = \frac{q\Delta t}{2m}(\mathbf{E}_{n+1} + \delta\mathbf{v}_{n+1/2} \times \mathbf{B}_n). \tag{16}$$

The solution is

$$\tilde{\mathbf{v}}_{n+1/2} = \frac{1}{1+\mathbf{\Theta}_I^2}(\mathbf{I} - \mathbf{\Theta}_I \times + \mathbf{\Theta}_I\mathbf{\Theta}_I) \cdot \mathbf{w}_n, \tag{17}$$

$$\delta\mathbf{v}_{n+1/2} = \frac{q\Delta t}{2m}\frac{1}{1+\mathbf{\Theta}_I^2}(\mathbf{I} - \mathbf{\Theta}_I \times + \mathbf{\Theta}_I\mathbf{\Theta}_I) \cdot \mathbf{E}_{n+1}, \tag{18}$$

where $\mathbf{\Theta}_I$ and $\mathbf{w}_n$ are defined by

$$\mathbf{\Theta}_I = + \frac{q\Delta t}{2m}\mathbf{B}_n(\mathbf{x}_n), \tag{19}$$

$$\mathbf{w}_n = \mathbf{v}_{n-1/2} + \frac{\Delta t}{2}\bar{\mathbf{a}}_{n-1} + \mathbf{v}_{n-1/2} \times \mathbf{\Theta}_I(\mathbf{x}_n). \tag{20}$$

The total velocity is

$$\mathbf{v}_{n+1/2} = \tilde{\mathbf{v}}_{n+1/2} + \delta\mathbf{v}_{n+1/2}. \tag{21}$$

The case $\Delta t > 0.4\omega_{ci}^{-1}$ corresponds to the gyrokinetic approach and is not treated in the present paper.

2.3. The electron guiding centre velocities

The electron guiding centre Eq. (6) is formally very similar to the full dynamic equation of motion. As we neglect the electron larmor radius, the electromagnetic field is considered at the position of the guiding centre. The charge density and the current assignments is done at the position of the guiding centre. The magnetic moment μ, which is the first adiabatic invariant, is supposed to be constant.

In order to eliminate the gyromotion of the particles around the magnetic field line, we introduce the implicit velocity $\bar{\mathbf{v}}$ in the term $\mathbf{v} \times \mathbf{B}(\mathbf{r})$ of Eq. (6). The gyromotion affects only the perpendicular component of the velocity. An implicit parallel acceleration $\bar{\mathbf{a}}_n$ is introduced in order to damp the parallel oscillations of the guiding centres that would give otherwise plasma fluctuations at the frequency ω_{pe}; it is defined by

$$\bar{\mathbf{a}}_n = \frac{1}{2}\left(\frac{q}{m}\mathbf{E}_{n+1} + \bar{\mathbf{a}}_{n-1}\right). \tag{22}$$

A discretized version of Eq. (6) must have the form

$$\mathbf{v}_{n+1/2} = \mathbf{v}_{n-1/2} + \Delta t\left[\bar{\mathbf{a}}_n - \frac{\mu}{m}\nabla B_n(\mathbf{x}_n) + \frac{q}{m}\mathbf{u}_n \times \mathbf{B}_n(\mathbf{x}_n)\right], \tag{23}$$

where $\mathbf{u}_n$ is a reasonable approximation of the perpendicular velocity at time n. The implicit velocity $\bar{\mathbf{v}}$ is introduced into the definition of $\mathbf{u}_n$ so as to damp the perpendicular gyromotion.

$$\mathbf{u}_n = \frac{1}{2}(\mathbf{v}_{n+1/2} + \bar{\mathbf{v}}_{n-1/2}), \tag{24}$$

$$\bar{\mathbf{v}}_{n-1/2} = \frac{1}{2}(\mathbf{v}_{n+1/2} + \bar{\mathbf{v}}_{n-3/2}). \tag{25}$$

Using quantities known at time step n, we cannot solve (23) because we do not know $\bar{\mathbf{a}}_n$ (this vector depends on $\mathbf{E}_{n+1}$ that is not yet computed). Therefore, the guiding centre velocity $\mathbf{v}_{n+1/2}$ is cut in a predicted part $\tilde{\mathbf{v}}_{n+1/2}$ and a correction $\delta\mathbf{v}_{n+1/2}$, that depend themselves on the prediction $\tilde{\bar{\mathbf{a}}}_n$ and the correction $\delta\bar{\mathbf{a}}_n$ of the implicit parallel acceleration $\bar{\mathbf{a}}_n$. Gathering Eqs. (23)–(25),

$$\begin{aligned}\tilde{\mathbf{v}}_{n+1/2} + \delta\mathbf{v}_{n+1/2} = \mathbf{v}_{n-1/2} + \frac{\Delta t}{2}\bar{\mathbf{a}}_{n-1} - \frac{\mu\Delta t}{m}\nabla B_n + \frac{q\Delta t}{4m}\bar{\mathbf{v}}_{n-3/2}\times\mathbf{B}_n(\mathbf{x}_n) - \tilde{\mathbf{v}}_{n+1/2}\times\boldsymbol{\Theta}_n(\mathbf{x}_n) + \frac{\Delta t}{2}\frac{q}{m}\mathbf{E}_{n+1} \\ - \delta\mathbf{v}_{n+1/2}\times\boldsymbol{\Theta}_n(\mathbf{x}_n),\end{aligned} \tag{26}$$

where $\boldsymbol{\Theta}$ defined by

$$\boldsymbol{\Theta} = \frac{3q\Delta t}{4m}\mathbf{B}_n(\mathbf{x}_n). \tag{27}$$

It is necessary to decide which parts of this equation come into the prediction, and which parts come into the correction. This question is addressed in Appendix A and the solution retained in this paper consists of a prediction that contains half of the electric acceleration in the parallel direction, and the full acceleration in the perpendicular direction,

$$\tilde{\mathbf{v}}_{n+1/2} = \mathbf{w}_n - \tilde{\mathbf{v}}_{n+1/2}\times\boldsymbol{\Theta}_n(\mathbf{x}_n). \tag{28}$$

The vector $\mathbf{w}_n$ is known at time step n and defined by

$$\mathbf{w}_n = \mathbf{v}_{n-1/2} + \frac{\Delta t}{2}[2\bar{\mathbf{a}}_{n-1} - (\bar{\mathbf{a}}_{n-1}\cdot\mathbf{b}_n)\mathbf{b}_n] - \frac{\mu\Delta t}{m}\nabla B_n + \frac{q\Delta t}{4m}\bar{\mathbf{v}}_{n-3/2}\times\mathbf{B}_n(\mathbf{x}_n). \tag{29}$$

The velocity correction contains the other terms

$$\delta\mathbf{v}_{n+1/2} = \frac{\Delta t}{2}\left[\frac{q}{m}\mathbf{E}_{n+1} - (\mathbf{I} - \mathbf{b}_n\mathbf{b}_n)\cdot\bar{\mathbf{a}}_{n-1}\right] + \delta\mathbf{v}_{n+1/2}\times\boldsymbol{\Theta}, \tag{30}$$

where $\mathbf{I}$ is the identity tensor, and $(\mathbf{b}_n\mathbf{b}_n)_{i,j} = b_i b_j$. Let us define

$$\mathbf{a}^*_{n-1} = (\mathbf{I} - \mathbf{b}_n\mathbf{b}_n)\cdot\bar{\mathbf{a}}_{n-1}, \tag{31}$$

the solutions of (28) and (30) are:

$$\tilde{\mathbf{v}}_{n+1/2} = \frac{1}{1+\boldsymbol{\Theta}^2}(\mathbf{I} - \boldsymbol{\Theta}\times + \boldsymbol{\Theta}\boldsymbol{\Theta})\cdot\mathbf{w}_n, \tag{32}$$

$$\delta\mathbf{v}_{n+1/2} = +\frac{q\Delta t}{2m}\frac{1}{1+\boldsymbol{\Theta}^2}(\mathbf{I} - \boldsymbol{\Theta}\times\boldsymbol{\Theta}\boldsymbol{\Theta})\cdot\left(\mathbf{E}_{n+1} - \frac{m}{q}\mathbf{a}^*_{n-1}\right). \tag{33}$$

The total velocity is

$$\mathbf{v}_{n+1/2} = \tilde{\mathbf{v}}_{n+1/2} + \delta\mathbf{v}_{n+1/2}. \tag{34}$$

The position of the electron guiding centres is the sum of a prediction and a correction

$$\mathbf{x}_{n+1} = \mathbf{x}_n + \Delta t\mathbf{v}_{n+1/2}, \tag{35}$$

$$\tilde{\mathbf{x}}_{n+1} = \mathbf{x}_n + \Delta t\tilde{\mathbf{v}}_{n+1/2}, \tag{36}$$

$$\delta\mathbf{x}_{n+1} = \Delta t\delta\mathbf{v}_{n+1/2}. \tag{37}$$

2.4. The charge density

The fields are coupled to the particles by the charge density and the current equations. The charge density assigned to the grid position $\mathbf{X}_j$ is

$$\rho_{n+1} = \sum_s q_s \sum_i S(\mathbf{X}_j - \mathbf{x}_{n+1}), \tag{38}$$

where S is the shape factor that relates the species s particle number i to the grid located at position $\mathbf{X}_j$.

2.5. General equations of the electric current

The current is the sum of the current carried by the ions, and the electron current. The ion current is derived from the velocities:

$$\mathbf{J}_{n+1/2,\mathrm{ion}} = q \sum_i \mathbf{v}_{n+1/2} \frac{1}{2} [S(\mathbf{X}_j - \mathbf{x}_n) + S(\mathbf{X}_j - \mathbf{x}_{n+1})], \tag{39}$$

with $q = +1$ for hydrogen ions. The electron current is the sum of the current $\mathbf{J}_{n+1/2,\mathrm{GC}}$ carried by the electron guiding centre velocities and the electron guiding centre magnetization current $\mathbf{J}_{n+1/2,M}$.

$$\mathbf{J}_{n+1/2,\mathrm{GC}} = q \sum_i \mathbf{v}_{n+1/2} \frac{1}{2} [S(\mathbf{X}_j - \mathbf{x}_n) + S(\mathbf{X}_j - \mathbf{x}_{n+1})], \tag{40}$$

with $q = -1$. The magnetization current $-\nabla \times \mu \mathbf{b}$ comes from the variation of magnetic field seen by the electrons during their gyromotion around their guiding centre. The vector $\mathbf{b} = \mathbf{B}/B$ is the magnetic field direction.

The magnetization current must even be retained when the electron Larmor radius is neglected in the equation of motion.

$$\mathbf{J}_{n+1/2,M} = -\sum_i \nabla \times \mu_i \mathbf{b}_{n+1/2}(\mathbf{x}_{n+1/2}) \frac{1}{2} [S(\mathbf{X}_j - \mathbf{x}_n) + S(\mathbf{X}_j - \mathbf{x}_{n+1})]. \tag{41}$$

The total current is

$$\mathbf{J}_{n+1/2} = \mathbf{J}_{n+1/2,\mathrm{ion}} + \mathbf{J}_{n+1/2,\mathrm{GC}} + \mathbf{J}_{n+1/2,M}. \tag{42}$$

2.6. The electric field equation

The field discretized Maxwell's equations can be rearranged to make an equation for $\mathbf{E}_{n+1}$ as a function of quantities that are known at time steps n and $n - 1/2$. Using (9), (7) and (8) yields

$$\mathbf{E}_{n+1} + \frac{\Delta t^2}{2} \nabla \times \nabla \times \mathbf{E}_{n+1} = \mathbf{E}_n + \Delta t \nabla \times \mathbf{B}_{n-1/2} - \frac{\Delta t^2}{2} \nabla \times \nabla \times \overline{\mathbf{E}}_{n-1} - \Delta t \mathbf{J}_{n+1/2}. \tag{43}$$

To get the electric field equation, we still have to express $\mathbf{J}_{n+1/2}$ in (43) as a function of $\mathbf{E}_{n+1}$ and known data. The current $\mathbf{J}_{n+1/2}$ comes from Eq. (42).

2.7. Contribution of the ion motions to the field equation

In the explicit case, the ion positions and velocities given by Eq. (12) do not depend on $\mathbf{E}_{n+1}$, the ion current (39) do not depend either on $\mathbf{E}_{n+1}$ and appears entirely in the right side of Eq. (43).

In the implicit case, following [8], the ion current consists of a prediction and a correction

$$\tilde{\mathbf{J}}_{n+1/2,\mathrm{ion}}(\mathbf{X}_j) = +q_{\mathrm{i}} \sum_i \tilde{\mathbf{v}}_{n+1/2} \frac{1}{2} [S(\mathbf{X}_j - \mathbf{x}_n) + S(\mathbf{X}_j - \tilde{\mathbf{x}}_{n+1})], \tag{44}$$

$$\delta \mathbf{J}_{n+1/2,\mathrm{ion}}(\mathbf{X}_j) = +q \sum_i \tilde{\mathbf{v}}_{n+1/2} \frac{1}{2} \boldsymbol{\delta}\mathbf{x} \cdot S(\mathbf{X}_j - \tilde{\mathbf{x}}_{n+1}). \tag{45}$$

After the use of simplified differencing, it is shown in [8] that

$$\delta\mathbf{J}_{n+1/2,\mathrm{ion}}(\mathbf{X}_j) = \frac{1}{\Delta t}\boldsymbol{\chi}_{\mathrm{ion}}\cdot\mathbf{E}_{n+1} - \nabla\times\Lambda_{\mathrm{ion}}\cdot\mathbf{E}_{n+1},$$

where

$$\boldsymbol{\chi}_{\mathrm{ion}} = \frac{q\Delta t^2}{2m}\tilde{\rho}_{\mathrm{ion}}\frac{1}{(1+\Theta_{\mathrm{I}}^2)}(\mathbf{I} - \boldsymbol{\Theta}_{\mathbf{I}}\times + \boldsymbol{\Theta}_{\mathbf{I}}\boldsymbol{\Theta}_{\mathbf{I}}), \tag{46}$$

$$\Lambda_{\mathrm{ion}} = +\frac{q^2\Delta t^2}{4m}\sum_{\mathrm{ion}}\tilde{\mathbf{v}}_{n+1/2}S(\mathbf{X}_j - \tilde{\mathbf{x}}_{n+1})\frac{1}{(1+\Theta_{\mathrm{I}}^2)}(\mathbf{I} - \boldsymbol{\Theta}_{\mathbf{I}}\times + \boldsymbol{\Theta}_{\mathbf{I}}\boldsymbol{\Theta}_{\mathbf{I}}). \tag{47}$$

The term that depend on Λ would be in Δt^3 in the electric field Eq. (43) and it is divided by the ion mass. Unlike Hewett and Langdon [8], we do not retain it in the current correction equation. We prefer to use the simpler form:

$$\delta\mathbf{J}_{n+1/2,\mathrm{ion}}(\mathbf{X}_j) = \frac{1}{\Delta t}\boldsymbol{\chi}_{\mathrm{ion}}\cdot\mathbf{E}_{n+1}. \tag{48}$$

2.8. Contribution of the electron guiding centre motions to the field equation

As the electron velocities and positions depend on $\mathbf{E}_{n+1}$, Eqs. (32)–(34), can be injected in (40), but the sum has to be done over the particles with a rotation tensor $(-\boldsymbol{\Theta}\times+\boldsymbol{\Theta}\boldsymbol{\Theta})$ that changes for every particle, as $\boldsymbol{\Theta}(\mathbf{x}_n)$ is defined for each particle. This is quite expensive, therefore, a different current calculation process is performed, called *simplified differencing* [8]. This approximation consists of neglecting the variation of the magnetic field over the cell containing the particle. Then, the rotation tensor is computed using $\boldsymbol{\Theta}_s$ defined at the grid location $\mathbf{X}_j$.

$$\boldsymbol{\Theta}_s = +\frac{3q\Delta t}{4m}\mathbf{B}_n(\mathbf{X}_j). \tag{49}$$

After some algebra [8] and the use of the simplified differencing approximation, it is possible to express $\mathbf{J}_{n+1/2,\mathrm{GC}}$ as

$$\mathbf{J}_{n+1/2} = \tilde{\mathbf{J}}_{n+1/2,\mathrm{GC}} + \delta\mathbf{J}_{n+1/2,\mathrm{GC}}, \tag{50}$$

with a prediction and a correction

$$\tilde{\mathbf{J}}_{n+1/2,\mathrm{GC}}(\mathbf{X}_j) = q\sum_i \tilde{\mathbf{v}}_{n+1/2}\frac{1}{2}[S(\mathbf{X}_j - \mathbf{x}_n) + S(\mathbf{X}_j - \tilde{\mathbf{x}}_{n+1})], \tag{51}$$

$$\delta\mathbf{J}_{n+1/2,\mathrm{GC}} = \sum_i +q[\delta\mathbf{v}_{n+1/2}S(\mathbf{X}_j - \tilde{\mathbf{x}}_{n+1}) \tag{52}$$

$$-\frac{1}{2}\nabla\times S(\mathbf{X}_j - \tilde{\mathbf{x}}_{n+1})[\tilde{\mathbf{v}}_{n+1/2}\times\boldsymbol{\delta}\mathbf{x}_{n+1}]]. \tag{53}$$

In the field Eq. (43), the electric current is multiplied by Δt. The terms proportional to a velocity introduce a new Δt factor. We limit ourselves to terms of the second order in Δt in the field equation, therefore, $\frac{1}{2}\nabla\times S(\mathbf{X}_j - \tilde{\mathbf{x}}_{n+1})[\tilde{\mathbf{v}}_{n+1/2}\times\delta\mathbf{x}_{n+1}]$ (or order 3 in the field equation) is neglected.

Using (33), the electron guiding centre current correction becomes

$$\delta\mathbf{J}_{n+1/2,\mathrm{GC}} = \sum_i \frac{q^2\Delta t}{2m}S(\mathbf{X}_j - \tilde{\mathbf{x}}_{n+1})\frac{(\mathbf{I} - \boldsymbol{\Theta}\times+\boldsymbol{\Theta}\boldsymbol{\Theta})}{(1+\Theta^2)}\cdot\left(\mathbf{E}_{n+1} - \frac{m}{q}\mathbf{a}^*_{n-1}\right). \tag{54}$$

Let us define the tensor $\boldsymbol{\chi}$

$$\boldsymbol{\chi} = \frac{q\Delta t^2}{2m}\tilde{\rho}_{\mathrm{GC}}\frac{1}{(1+\Theta^2)}(\mathbf{I} - \boldsymbol{\Theta}\times+\boldsymbol{\Theta}\boldsymbol{\Theta}) \tag{55}$$

and the vector $\mathbf{J}^*$,

$$\mathbf{J}^* = \frac{q^2\Delta t}{2m}\frac{1}{(1+\Theta^2)}(\mathbf{I}-\boldsymbol{\Theta}\times+\boldsymbol{\Theta}\boldsymbol{\Theta})\cdot\sum_i S(\mathbf{X}_j-\tilde{\mathbf{x}}_{n+1})\left(-\frac{m}{q}\right)\mathbf{a}^*_{n-1}. \tag{56}$$

The guiding centre current correction writes

$$\delta\mathbf{J}_{n+1/2,\mathrm{GC}} = \frac{1}{\Delta t}\boldsymbol{\chi}\cdot\mathbf{E}_{n+1}+\mathbf{J}^*. \tag{57}$$

2.9. Contribution of the magnetization current to the field equation

In the electron guiding centre magnetization current (41), the dependence on $\mathbf{E}_{n+1}$ is linked to those of $\mathbf{b}_{n+1/2}$ stated in (59). The dependence of $\mathbf{b}_{n+1/2}$ on the future electric field is approximated through a linear expansion in $\mathbf{E}_{n+1}$. From (7) and (8),

$$\mathbf{B}_{n+1/2} = \mathbf{B}_{n-1/2}-\frac{\Delta t}{2}\nabla\times\overline{\mathbf{E}}_{n-1}-\frac{\Delta t}{2}\nabla\times\mathbf{E}_{n+1}. \tag{58}$$

Let $\mathbf{B}^* = \mathbf{B}_{n-1/2}-(\Delta t/2)\nabla\times\overline{\mathbf{E}}_{\mathbf{n-1}}$ and $\tilde{\mathbf{b}} = \mathbf{B}^*/B^*$. To the first order in $\nabla\times\mathbf{E}_{n+1}$,

$$\mathbf{b}_{n+1/2} = \tilde{\mathbf{b}}-\frac{\Delta t}{2B^*}(\mathbf{I}-\tilde{\mathbf{b}}\tilde{\mathbf{b}})\cdot\nabla\times\mathbf{E}_{n+1} \tag{59}$$

and $\tilde{\mathbf{b}}$ is a prediction of the magnetic field direction, the other part of the right-hand side of (59) is the correction. Therefore Eqs. (41) and (59) give the magnetization current:

$$\begin{aligned}\mathbf{J}_{n+1/2,M} &= -\sum_i \nabla\times\frac{\mu_i}{2}\left[\tilde{\mathbf{b}}-\frac{\Delta t}{2B^*}(\mathbf{I}-\tilde{\mathbf{b}}\tilde{\mathbf{b}})\cdot\nabla\times\mathbf{E}_{n+1}\right][S(\mathbf{X}_j-\mathbf{x}_n)+S(\mathbf{X}_j-\mathbf{x}_{n+1})]\\ &= -\sum_i \nabla\times\mu_i\tilde{\mathbf{b}}\frac{1}{2}[S(\mathbf{X}_j-\mathbf{x}_n)+S(\mathbf{X}_j-\tilde{\mathbf{x}}_{n+1})-\delta\mathbf{x}\cdot\nabla S(\mathbf{X}_j-\tilde{\mathbf{x}}_{n+1})]-\sum_i\nabla\times\mu_i\\ &\quad\times\frac{1}{2}\left[-\frac{c\Delta t}{2B^*}(\mathbf{I}-\tilde{\mathbf{b}}\tilde{\mathbf{b}})\cdot\nabla\times\mathbf{E}_{n+1}\right][S(\mathbf{X}_j-\mathbf{x}_n)+S(\mathbf{X}_j-\tilde{\mathbf{x}}_{n+1})].\end{aligned} \tag{60}$$

The magnetization current can then be cut in a predicted part $\tilde{\mathbf{J}}_{n+1/2}$ that do not depend on the future electric field and a correction part $\delta\mathbf{J}_{n+1/2}$ that is linearly dependent on $\mathbf{E}_{n+1}$.

$$\mathbf{J}_{n+1/2,M} = \tilde{\mathbf{J}}_{n+1/2,M}+\delta\mathbf{J}_{n+1/2}. \tag{61}$$

The validity of the linear approximation requires $\tilde{\mathbf{J}}_{n+1/2}\gg\delta\mathbf{J}_{n+1/2}$.

$$\tilde{\mathbf{J}}_{n+1/2,M} = -\sum_i\nabla\times\frac{\mu_i}{2}\tilde{\mathbf{b}}[S(\mathbf{X}_j-\mathbf{x}_n)+S(\mathbf{X}_j-\tilde{\mathbf{x}}_{n+1})], \tag{62}$$

$$\begin{aligned}\delta\mathbf{J}_{n+1/2,M} &= \sum_{\mathrm{GC}}\nabla\times\mu_i\frac{1}{2}\frac{\Delta t}{2B^*}(\mathbf{I}-\tilde{\mathbf{b}}\tilde{\mathbf{b}})\cdot(\nabla\times\mathbf{E}_{n+1})[S(\mathbf{X}_j-\mathbf{x}_n)+S(\mathbf{X}_j-\tilde{\mathbf{x}}_{n+1})]\\ &\quad+\frac{\mu}{2}[(\delta\mathbf{x}_{n+1}\cdot\nabla)\nabla S\times\tilde{\mathbf{b}}+(\delta\mathbf{x}_{n+1}\cdot\nabla S)\nabla\times\tilde{\mathbf{b}}].\end{aligned} \tag{63}$$

After some algebra, the current correction is written

$$\delta\mathbf{J}_{n+1/2,M} = \frac{\Delta t}{2}\nabla\times(\boldsymbol{\Gamma}\cdot(\nabla\times\mathbf{E}_{n+1}))+\boldsymbol{\chi}_M\cdot\mathbf{E}+\mathbf{J}_M, \tag{64}$$

where $\boldsymbol{\Gamma}$ and $\boldsymbol{\chi}_M$ are the tensor fields defined on the simulation grid by

$$\boldsymbol{\Gamma} = \sum_i\frac{\mu_{\mathrm{i}}}{2B^*}(\mathbf{I}-\tilde{\mathbf{b}}\tilde{\mathbf{b}})[S(\mathbf{X}_j-\mathbf{x}_n)+S(\mathbf{X}_j-\tilde{\mathbf{x}}_{n+1})], \tag{65}$$

$$\boldsymbol{\chi}_M = -\sum_i\frac{\mu_{\mathrm{i}}\partial^2_{xy}S}{2}\tilde{\mathbf{b}}\times\frac{\boldsymbol{\chi}}{\tilde{\rho}}\cdot+\sum_i\nabla\times\tilde{\mathbf{b}}\frac{\mu_{\mathrm{i}}}{2}\nabla S\cdot\left(\frac{\boldsymbol{\chi}}{\tilde{\rho}}\right) \tag{66}$$

and $\mathbf{J}_M$ is a vector field defined by

$$\mathbf{J}_M = \sum_i \frac{\mu_i \partial^2_{xy} S}{2} \frac{\mathbf{J}^*}{\tilde{\rho}} \times \tilde{\mathbf{b}} + \left(\sum_i \frac{\mu_i}{2} \right) \left(\nabla S \cdot \frac{\mathbf{J}^*}{\tilde{\rho}} \right) \nabla \times \tilde{\mathbf{b}}. \tag{67}$$

The fields $\mathbf{B}^*, \tilde{\mathbf{b}}, B^*$ must be derived at the position x_i of each particle. This is quite expensive, therefore, the *simplified differencing* [7] is applied again. Then, the $\mathbf{\Gamma}$ tensor is computed using $\mathbf{B}^*, \tilde{\mathbf{b}}, B^*$ at the grid location $\mathbf{X}_j$.

2.10. Final form of the electric field equation

Injecting Eqs. (42, 48, 50, 54, 61, 62, 64) into (43), we find a new electric field equation

$$(\mathbf{I} + \boldsymbol{\chi}_{\text{ion}} + \boldsymbol{\chi}) \cdot \mathbf{E}_{n+1} + \frac{\Delta t^2}{2} [\nabla \times (\mathbf{I} + \mathbf{\Gamma})] \cdot (\nabla \times \mathbf{E}_{n+1}) = \mathbf{Q}, \tag{68}$$

$$\mathbf{Q}' = \mathbf{E}_n + \Delta t \nabla \times \mathbf{B}_{n-1/2} - \frac{\Delta t^2}{2} \nabla \times \nabla \times \overline{\mathbf{E}}_{n-1} - \Delta t (\tilde{\mathbf{J}}_{n+1/2,ion} + \tilde{\mathbf{J}}_{n+1/2,\text{GC}} + \mathbf{J}^* + \tilde{\mathbf{J}}_{n+1/2,M}), \tag{69}$$

where a priori, $\mathbf{Q} = \mathbf{Q}'$.

2.11. Poisson correction

The electric field must be a solution of the Poisson equation $\nabla \cdot \mathbf{E}_{n+1} = \rho_{n+1}$. Taking the divergence of Eq. (69) gives $\nabla \cdot \mathbf{E}_{n+1} = \nabla \cdot \mathbf{Q}'$. Generally $\nabla \cdot \mathbf{Q}' \neq \rho_{n+1}$ and the solution $\mathbf{E}$ of $\mathbf{Q} = \mathbf{Q}'$ does not check the Poisson equation. Hence, a correction must be added to $\mathbf{E}$. This correction is due to charge density effects and is therefore of electrostatic nature. Let $\mathbf{E}_{n+1} = \mathbf{E} - \nabla \Psi$ be the electric field that checks both the Poisson equation and (69). The potential Ψ is the solution of

$$\nabla \cdot (\mathbf{I} + \boldsymbol{\chi}_{\text{ion}} + \boldsymbol{\chi}) \cdot \nabla \Psi = \nabla \cdot (\mathbf{Q}' + \Delta t \mathbf{J}^*) - \tilde{\rho}_{n+1}. \tag{70}$$

Therefore the electric field $\mathbf{E}_{n+1}$ at time step $n+1$ is the difference of the solutions of the field equation $\mathbf{Q} = \mathbf{Q}'$, and of $\nabla \Psi$ given by (70). The demonstration of (70) is given in Appendix B.

3. Tests and applications

A numerical simulation code has been developed following the above algorithm. This is a 2D code where all the electromagnetic and velocity fields have three components. It is periodic in both directions. A few validation tests are presented in this section. All the validation tests presented in this paper were run on a laptop personal computer.

3.1. Propagation of low frequency waves

We present two propagation tests of non compressional low frequency (quasi-MHD) waves, in two regimes of plasma. In the bi-fluid cold plasma approximation used to prepare these simulations, these modes are undamped.

The first example corresponds to the propagation of a single non compressive right-hand circularly polarized wave mode. In MHD, this would correspond to the fast magnetosonic mode. It is not compressional because it propagates along the magnetic field. The polarization coefficients for the initialization are computed using the cold plasma bi-fluid equations. (The dispersion and polarization equations are detailed in Appendix C.)

The magnetic field is given by $\omega_{ce}/\omega_{pe} = 0.2$, the mass ratio (1836) is those of protons and electrons, the thermal velocities correspond to cold electrons, $v_{te} = 1. \times 10^{-3}$, but warmer protons, $v_{ti} = 2.3 \times 10^{-3}$. The simulation box is almost 1D, with $512 * 4$ cells, $\Delta x = 0.5$, and the time step is $\Delta t = 10$. There are 20 particles per cell. The wavelength is significantly shorter than for MHD waves, and the theoretical phase velocity of the

wave is $V_\phi = 7.7 \times 10^{-3}$, quite above the Alfvén velocity $V_A = 4.7 \times 10^{-3}$. The amplitude of the perturbation is given by the ratio $\delta B/B_0 = 1. \times 10^{-2}$, where B_0 is the ambient magnetic field. This correspond to a low level of signal, and this simulation, if noisy, shows that a low level perturbation can propagate without being disturbed by the numerical noise.

We observe that the Alfvén wave propagates with the right velocity $V_\phi = 7.68 \times 10^{-3}$ (Fig. 1), and an electric to magnetic amplitudes ratio $E/B = 7.50 \times 10^{-3}$ that is very close to the theoretical value.

An another test has been made, with the parallel propagation of a left-hand circularly polarized wave in a 2D simulation domain. The magnetic field is given by $\omega_{ce}/\omega_{pe} = 8$, the mass ratio (1836) is those of protons and electrons, the thermal velocities is $v_{te} = 0.01$, and $T_i = T_e$. The 2D simulation box has $256 * 128$ cells, $\Delta x = 4$, and the time step is $\Delta t = 10$. The wavelength is shorter than for MHD waves, and the theoretical velocity of the wave, $V_\phi = 0.1618$ (deduced from bi-fluid equations), is below the Alfvén velocity $V_A = 0.1867$. Here again, the amplitude of the perturbation is given by the ratio $\delta B/B_0 = 1. \times 10^{-2}$, but in the present case, B_0 is 40 times higher than in the previous (rather noisy) simulation. Therefore, the wave amplitude is well above the noise level. No wave damping is evidenced in the simulation.

We observe that the Alfvén wave propagates with the velocity $V_\phi = 0.156$ (Fig. 2), and an electric to magnetic amplitudes ratio $E/B = 0.156$. These values are close to the theoretical prediction (0.162).

3.2. Compressive perturbation of the plasma

A perturbation with a wavelength $\lambda = 122$, of arbitrary magnetic and longitudinal velocity amplitudes is used to start a quasi-1D simulation of a plasma with a magnetic field $B = 2$ or $B = 0.4$, $v_{te} = 0.01$, $v_{ti} = 2.3 \times 10^{-4}$. The perturbation consists of a sinusoidal perpendicular magnetic field δB of amplitude $\delta B/B_0 = 1. \times 10^{-2}$ and a sinusoidal mean parallel electron velocity of amplitude $\delta v_{xe}/v_{te} = 5 \times 10^{-2}$. The ratio of amplitudes and the phases of these two perturbations do not correspond to a peculiar wave mode; therefore, all the possible modes of wavelength $\lambda = 122$ could appear in the simulation. The simulations are run over 2048 time steps, with $\Delta t = 20$. The grid size is 512×4, $\Delta x = 0.24$, there are 50 macroparticles per cell.

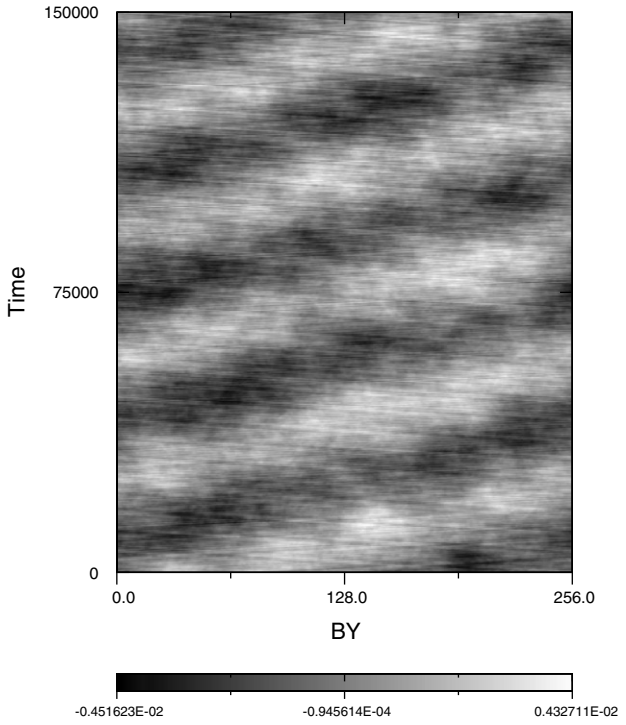

Fig. 1. Propagation of a right-hand circularly polarized Alfvén wave of very low amplitude. Magnetic field B_y as a function of position along the direction x of the external magnetic field and time.

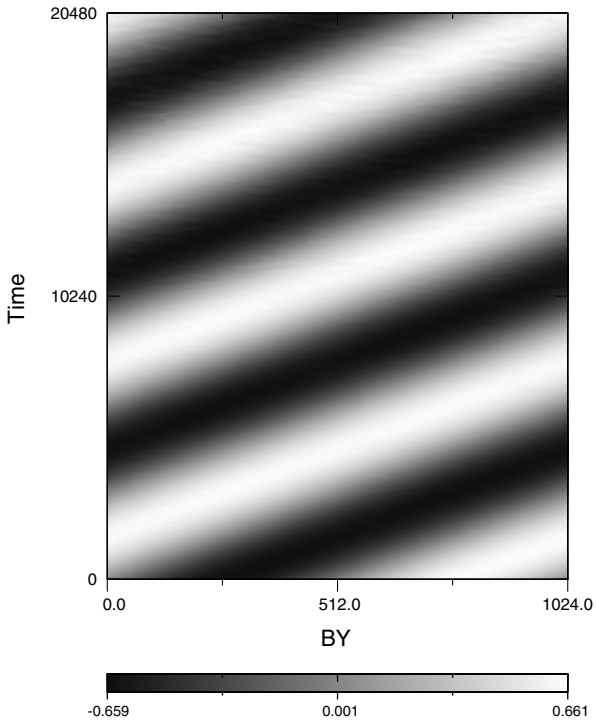

Fig. 2. Propagation of a left-hand circularly polarized Alfvén wave. Magnetic field B_y as a function of position along the direction x of the external magnetic field and time.

At $X = 2$ (position chosen arbitrarily), time series of the electric, magnetic and density fields are recorded and Fourier transformed. Fig. 3 displays an example of frequency spectrums of time series taken at arbitrary points in the simulation domain. Two frequencies generally appear. It means that the perturbation of wavelength λ is projected on two proper modes of the plasma that have the same wavelength. We have compared these two modes frequencies with those given for the same plasma and the same wavelength by the Whamp [13] program that solves semi-analytically the linear dispersion relation of the plasma. We have made a few simulations with different angles $\theta = (\mathbf{k}, \mathbf{B}_0)$. The results are summarized in Table 1. We can notice that the frequencies in the simulation fit the frequencies linearly predicted by the Whamp program.

3.3. Ion–ion instability and plasma filamentation

Some numerical studies have been devoted to the interaction between an ion beam and a plasma in the highly magnetized plasma of the Earth auroral zone magnetosphere. The linear and the nonlinear study of the instability triggered by a fast ion beam had first been conducted with an explicit electrostatic code [14]. Beam ions were shown to generate oblique waves. The nonlinear beating between these oblique waves produces purely transverse waves that lead to a strong modulation of the density and of the electrostatic potential. This study was later reproduced [10] with an electron guiding centre electromagnetic code (a code explicit in ω_{pe}) in a simulation using the same spatial resolution, but a larger time step. The electrostatic character of this instability was confirmed.

The magnetic field, parallel to the x axis, is given by the ratio $\omega_{ce}/\omega_{pe} = 8.0$ The electron thermal velocity is $v_{te} = 0.143 \times 10^{-2}$, the ion thermal velocity is $v_{ti} = 0.2 \times 10^{-4}$ for the background population and $v_{tb} = 0.65 \times 10^{-4}$ for the beam. The ion to electron mass ratio is $m_i/m_e = 100$. The mean velocity is 0 for the background ions, 0.2×10^{-2} for the ion beam. The mean electron velocity is 0.1×10^{-2} so as to avoid any current density in the initial conditions. The computation is performed on a numerical grid of size 256×128, each grid cell has a size $\Delta x = 0.2 \times 10^{-2}$ and there are 30 particles of each species per cell (15 background ions and 15 beam ions). The time step is $\Delta t = 0.4$.

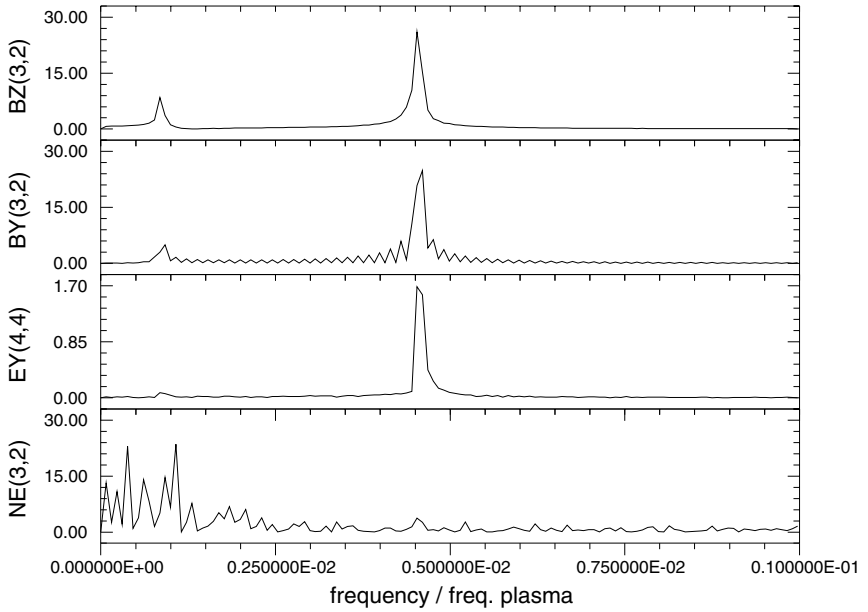

Fig. 3. Propagation of a compressional wave. Frequency spectrum of the magnetic field Y and Z components, of the electric field Y component and of the density taken at arbitrary points in the simulation box. These spectrums are derived from the simulation "c" (see Table 1) of compressional modes.

Table 1
Frequencies of compressive modes, for various magnetic field amplitudes and wave-magnetic field angles

Run	B	θ	ω Whamp	ω simulation
a	2	90	0.236×10^{-2}	0.23–0.24×10^{-2}
b	2	75	0.053×10^{-2}	0.05–0.06×10^{-2}
b	2	75	0.27×10^{-2}	0.27×10^{-2}
c	2	45	0.086×10^{-2}	0.08×10^{-2}
c	2	45	0.45×10^{-2}	0.45–0.46×10^{-2}
d	2	0	0.092×10^{-2}	0.09×10^{-2}
d	2	0	0.60×10^{-2}	0.58×10^{-2}
e	0.4	60	0.073×10^{-2}	0.075×10^{-2}
e	0.4	60	0.015×10^{-2}	0.015×10^{-2}
f	0.4	0	0.122×10^{-2}	0.126×10^{-2}
f	0.4	0	0.018×10^{-2}	0.019×10^{-2}

Comparison of the values deduced from the linear theory (Whamp program) and from our simulations.

Fig. 4 shows the evolution of electrostatic and magnetic energies. The shape of the curve of electrostatic energy is similar to those presented in [14,10]. The first phase of the simulation is dominated by noise (because of the low number of particles in the simulation) up to time 500 where the electrostatic energy goes above the noise level. From time 500 to 800, the growth of the electrostatic energy is exponential. The maximum of the electrostatic energy is reached at time 800, followed by a decrease from time 800 to 1300. The comparison of the electrostatic to the magnetic energy lead to a characteristic ratio $E/B = 10^5$ which confirm the higly electrostatic character of this instability.

Fig. 5 shows the transverse component E_y of the electric field at times 800, 1920, and 3200. At time 800, corresponding to the maximum level of the linear instability, the electric field is dominated by oblique ion cyclotron waves with wave vectors $\mathbf{k}_x \pm \mathbf{k}_y$ where $k_y/k_x = \tan 77^\circ$. At time 3200, the ion cyclotron waves have decayed, and the plasma is filamented. The plot at time 1920 corresponds to an intermediate case where both decaying ion cyclotron waves, and amplified transverse waves are observed. The thickness of the filaments and the figures shown in this section are the same as in the two previous studies [14,10].

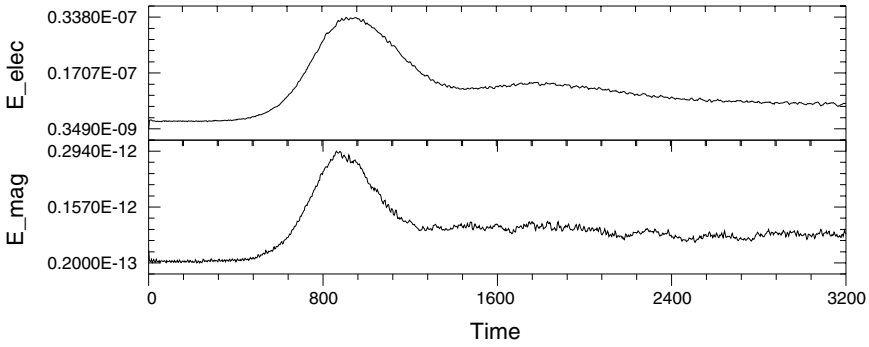

Fig. 4. Electric and magnetic energies in the ion–ion instability simulation.

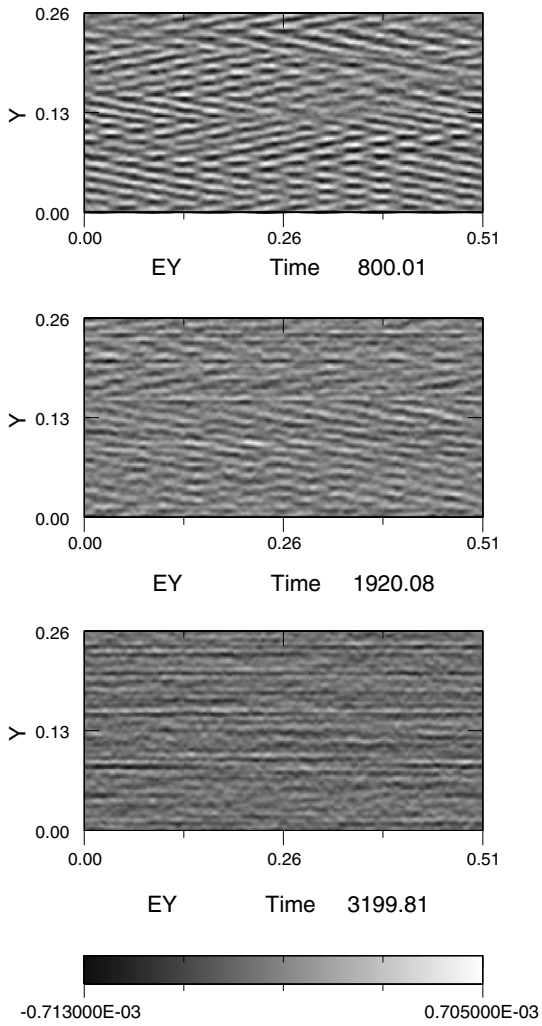

Fig. 5. Electric field Y component in the ion–ion instability simulation. This component lies in the plane of the simulation domain and is perpendicular to the ambient magnetic field.

Because of the constraints $\omega_{pe} < 0.4$ on the time step, and because of the dependency of time scales of the instability with the ion mass, the two previous studies where conducted with a reduced ion to electron mass

ratio $m_p/m_e = 100$. The present code, because of the need of describing the ion Larmor radius ρ_i, was constrained to a rather small cell size, and consequently (Courant condition), to a small time step. With the present code, it is much easier to simulate the ion–ion instability in similar conditions, but with a realistic mass ratio $m_p/m_e = 1836$. In that case, as ρ_i is larger, $\Delta x = 0.8 \times 10^{-2}$ (four times larger as in the previous simulation) and $\Delta t = 4$ (10 times larger as in the previous simulation, and 80 times larger than in the explicit electron full dynamics simulation [14]) are possible. We have run such a simulation. We would not describe it into detail, because a direct comparison with previous data is not possible, and therefore cannot contribute to validate or invalidate the present code. But we can briefly summary what happens: the same oblique instability develops, and when the nonlinear phase of the instability is reached (around time 8000), a strictly perpendicular mode appears, but with less intensity than in the case of a reduced mass ratio.

3.4. Ion-temperature anisotropy instabilities

We consider mirror and ion cyclotron instabilities triggered by an ion-temperature anisotropy.

The plasma is unstable to the mirror mode in the case of a large perpendicular temperature, $T_\perp/T_\parallel - 1 > 1/\beta$, where the temperatures and the plasma β refer to the ion species. This approximation is valid when $\beta \gg 1$ and the unstable modes correspond to quasi-perpendicular wave vectors with $k_\perp \rho_L \sim 0.5$, where ρ_L is the ion Larmor radius. The real frequency is equal to zero, the growth rate is proportional to $k_\parallel$ and the magnetic field and the density are anti-correlated. For smaller values of β, the mirror mode occurs for oblique wave vectors. It can occur at inclinasion angles $\theta = (\mathbf{k}, \mathbf{B}_0)$ down to 45°.

The ion cyclotron instability is easier to trigger, it has a finite frequency and propagates preferentially in the parallel direction.

We have set a simulation with the following plasma values: The magnetic field $B = (B\cos(\theta), B\sin(\theta), 0)$ is given by $\omega_{ce}/\omega_{pe} = 0.1$ and $\theta = 65°$. The electron distribution is isotropic and $v_{te} = 10^{-3}$. The ions are anisotropic with a parallel thermal velocity $v_{t\parallel} = 7 \times 10^{-4}$ and a perpendicular thermal velocity $v_{t\perp} = 2.5 v_{t\parallel}$. The size of a cell is $\Delta x = 0.5$, the time step is $\Delta t = 25$. The simulation box is pseudo 1D, with a grid size 2048×4 and there are 100 particles per cell. The physical length of the box, $L_x = 1024$ allows for wave vectors that are multiples of $k_0 = 0.613 \times 10^{-2}$.

A linear computation provided by the Whamp program shows that for $\theta = 65°$, there are two instabilities in competition. The stronger is the ion cyclotron wave (ICW) instability, with a wavelength $l_{ICW,Whamp} \sim 160$–180, i.e. $3.4 \times 10^{-2} \leqslant k_{ICW,Whamp} \leqslant 3.9 \times 10^{-2}$, a frequency $\omega_{ICW,Whamp} = 3.9 \times 10^{-5}$ and a growth rate rather constant over this domain of wavelengths $\gamma_{ICW,Whamp} = 3.4 \times 10^{-6}$. The signature of this mode is stronger on the B_z component of the magnetic field (this component is perpendicular both to the magnetic field and the wave vector). There is also a mirror mode characterized by a null frequency, a perturbation of the magnetic field (mostly visible on the B_y component) anti-correlated with the density fluctuations. Its wavelength is $l_{M,Whamp} = 300$, i.e. $k_{M,Whamp} = 2.45 \times 10^{-2}$, its real frequency is null and its growth rate is $\gamma_{M,Whamp} = 1.8 \times 10^{-6}$.

A space–time fourier transform (FT) of $B_z(x,t)$ is shown on top of Fig. 6. (The FT is made on $B_y(x,t)$ for x over all the simulation box, and for $3.7 \times 10^5 < t < 7.5 \times 10^5$ i.e. in the last half of the simulation, when the most unstable modes dominate the plasma.) We can see that the dominant mode corresponds to $3.1 \times 10^{-2} \leqslant k \leqslant 3.6 \times 10^{-2}$ (mode number $n = 6$, wavelength $l = 170$) and $3.9 \times 10^{-5} \leqslant \omega \leqslant 4.6 \times 10^{-5}$. The lower part of Fig. 6 shows the time evolution of this mode's amplitude (in log scale). The straight line is derived from the theoretical value $\gamma_{ICW,Whamp}$ of the growth rate. We can see that the values of the most unstable wave vector, the real frequency, and the growth rate given by the simulation are consistent with those given by the (Whamp) theoretical linear analysis.

But the ICW is not the only unstable mode. As computed with Whamp, the B_y component should show the existence of the mirror instability. A space–time Fourier transform (FT) of $B_y(x,t)$ is shown on top of Fig. 7. We can see that the dominant mode corresponds to $1.8 \times 10^{-2} \leqslant k \leqslant 2.4 \times 10^{-2}$ (mode number $n = 4$, wavelength $l = 256$) and $0 \leqslant \omega \leqslant 7 \times 10^{-6}$. The time evolution of the most intense mode ($n = 4$) is shown in the lower part of Fig. 7. The superimposed straight line is derived from its theoretical growth rate $\gamma_{M,Whamp}$. We can notice that the order of magnitude of the growth rate in the simulation is the same as those of the theoretical prediction, but the fit is less accurate than with the (dominant) ICW instability. This may be

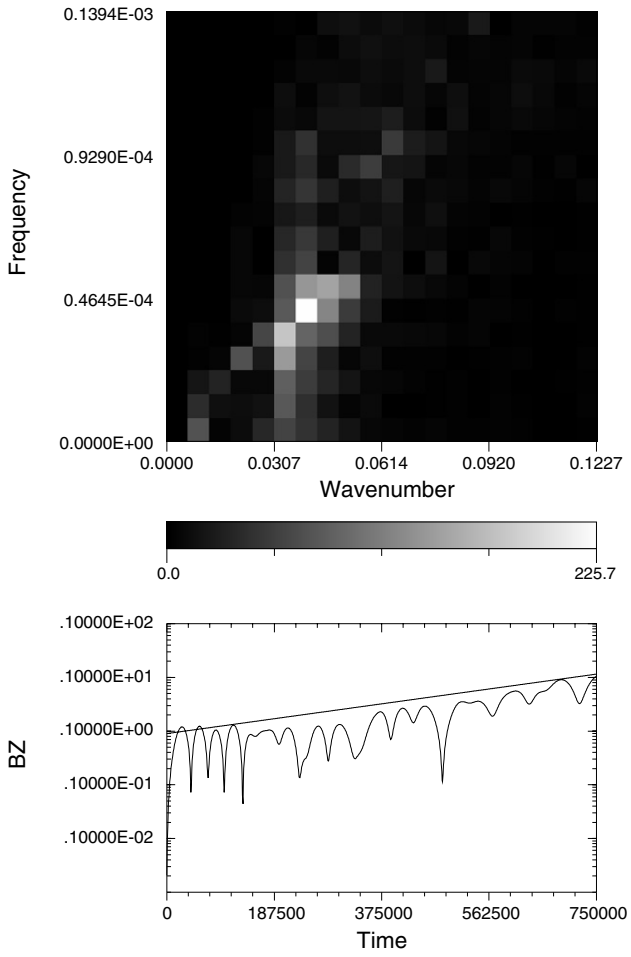

Fig. 6. Ion-temperature anisotropy simulation. Top: Amplitude of the space–time Fourier transform of the magnetic field Z component $B_z(x,t)$. The B_z component is perpendicular to the simulation box and to the ambient magnetic field. Bottom: Time evolution of the most unstable B_z mode ($n = 6$), superimposed with the theoretical prediction (Whamp) deduced from the growth rate $\gamma_{\mathrm{ICW,Whamp}}$ for the mirror instability.

due to electron temperature effects, as the electron temperature is modified by the growth of the ICW instability. (A precise study of this effect is beyond the scope of the present paper.) The values of the most unstable wave vector, the real frequency, and the growth rate given by the simulation are nevertheless consistent with the theoretical values $k_{\mathrm{M,Whamp}}$, $\omega_{\mathrm{M,Whamp}} = 0$ and $\gamma_{\mathrm{M,Whamp}}$ given for the mirror mode.

We can see also on the top of Fig. 7 that the modes associated to the ion cyclotron instability (the same as in Fig. 6) are visible. This is compatible with the polarization given by Whamp: the ion cyclotron modes are visible on both B_y and B_z while the mirror mode only appears on B_y.

3.5. Sheared flow instability

We set initially a rectangular domain with a uniform magnetic field, a uniform density, a uniform temperature, and a shear of plasma mean velocity. The grid size is 256×128 and $\Delta x = 0.5$. There are 80 macroparticles per cell. The ion to electron mass ratio is reduced to $m_{\mathrm{i}}/m_{\mathrm{e}} = 100$. The timestep $\Delta t = 10$. The magnetic field is perpendicular to the simulation grid $B = B_z$, $\omega_{\mathrm{ce}}/\omega_{\mathrm{pe}} = 0.1$. The electron thermal velocity is $v_{\mathrm{te}}/c = 0.05$ and $T_{\mathrm{i}} = T_{\mathrm{e}}$. There are actually two shears of mean electron and ion velocity, in order to fit bi-periodic boundaries conditions; the velocity profile is given by $v(y) = v_0\{\tanh[(y - y_1)/d_1] - \tanh[(y - y_2)/d_2]\}$ with $d1 = d_2 = 8\Delta x$, $y_1 = 32\Delta x$ and $y_2 = 64\Delta x$. When $v_0 = 3v_{\mathrm{ti}}$, the simulation shows that the layer is unstable. The magnetic field

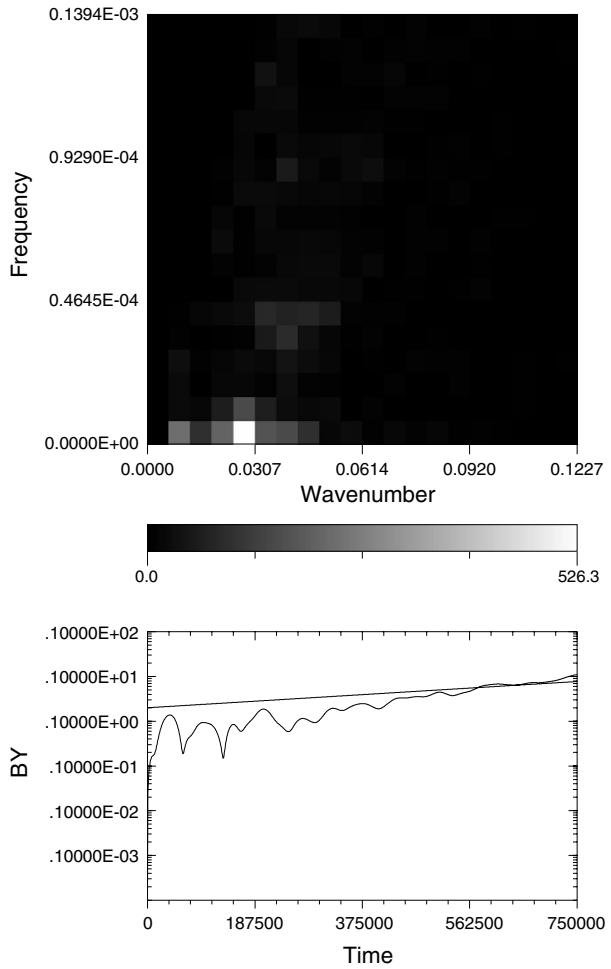

Fig. 7. Ion-temperature anisotropy simulation. Top: Amplitude of the space–time Fourier transform of the magnetic field Y component $B_y(x,t)$. The B_y component is perpendicular to the simulation box, and therefore, to the wave vectors ($k = k_x$). Bottom: Time evolution of the most unstable B_y mode ($n = 4$), superimposed with the theoretical prediction (Whamp) deduced from the growth rate $\gamma_{\mathrm{M,Whamp}}$ for the ICW instability.

$B_z(x,y)$ at three different times is displayed in Fig. 8. We can see the development of a perturbation along the velocity shear direction. It shows that the velocity shear layer is rather strongly destabilized by a surface-wave-like structure. According to the prediction on the MHD Kelvin–Helmhotz instability, a magnetic field parallel to the sheared flow would tend to stabilize it. We have set an another simulation where initially, the magnetic field $B = B_x$ is uniform and parallel to the sheared flow. The other parameters are the same as in the previous simulation. The magnetic field has no significant perturbation (not shown). The velocity shear instability is actually stabilized in our simulation by a magnetic field parallel to the sheared flow.

4. Choice of parameters for convergence

Implicit codes are designed to allow for larger time steps and grid sizes. Nevertheless, some conditions for stability and accuracy are still necessary. As the present algorithm have been described in terms of time integration, the conditions on the time step are the easiest to derive. The implicitness on the electron plasma oscillation allows for $\Delta t\omega_{\mathrm{pe}} \gtrsim 1$, and if the ion implicit solver is implemented, $\Delta t\omega_{\mathrm{pi}} \gtrsim 1$. In codes dealing with full electron dynamics and using the Boris algorithm [11], the condition $\Delta t\omega_{\mathrm{ce}} < 1$ is required, not for stability, but for accuracy, even if in some cases, correct results can be attained when this prescription is violated [15].

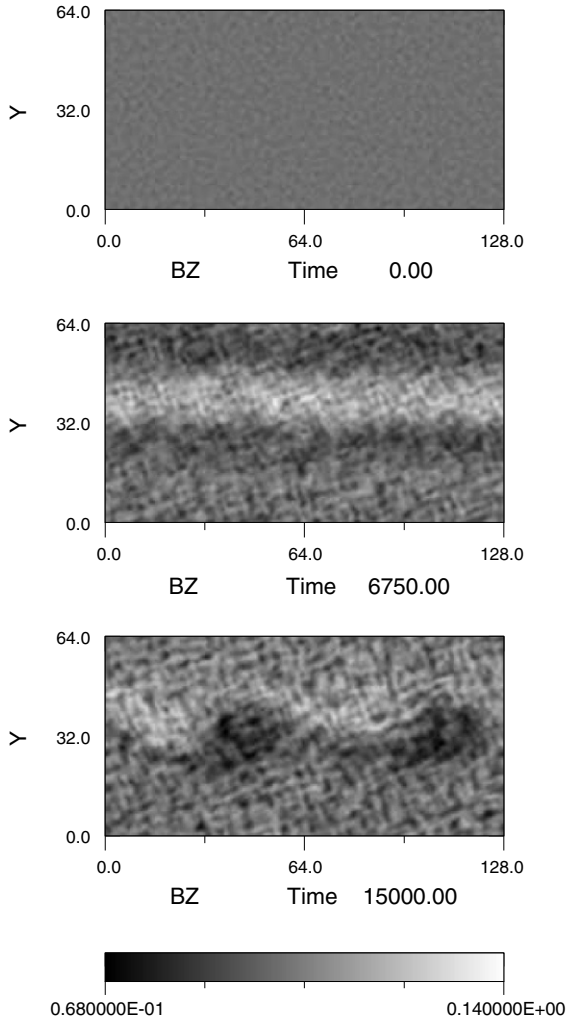

Fig. 8. Magnetic field Z component $B_z(x, y)$ in the velocity shear instability simulation where initially, $B = B_z$ is orthogonal to the sheared flow.

As we deal with electron guiding centres, the inverse condition

$$\Delta t \omega_{ce} > 1 \tag{71}$$

is *required* for accuracy; this is the only requirement for a large time step. As in every standard particle in cell code, for stability, the computation of the charge and current densities requires $v_{te}\Delta t < \Delta x$ and $v_{ti}\Delta t < \Delta x$. The consideration of the finite grid instability may restrict the above conditions [4]. The limiting conditions for the choice of the grid size are less obvious, they must be deduced as the counterparts of those concerning time integration.

Let us consider the implicitness of the code upon the electron plasma frequency. It means that the high frequency fluctuations associated to the thermal noise is damped. This thermal noise is electrostatic in nature and is caused by small displacements of the electrons. Spatially, the consideration of these small displacements lead, if we deal with a real plasma, to the concept of screening effect, characterized by the Debye length, $\lambda_D = v_{te}/\omega_{pe}$. When space and time effect are considered altogether (for propagating waves for instance), we see that the Debye length appears only in relations, such as the Bohm and Gross dispersion relation, where the typical frequency is close to ω_{pe}. Therefore, as in [7,8], for the stability of the algorithm, it is not needed to resolve spatially the Debye length, λ_D. We can have $\Delta x > \lambda_D$.

Do we have to resolve the electron inertial length c/ω_{pe}? The inertial length appears as soon as one consider the finiteness of the mass of the electrons (we do that), and the polarization current in the Ampere equation (we do that too). Contrary to the Debye length, the electron inertial length does not only appears in the dispersion relation of high frequency modes. It also acts in the propagation of low frequency waves, such as the inertial Alfvén wave. Therefore, the electron inertial length must be resolved, and necessarily:

$$\Delta x < c/\omega_{pe}. \tag{72}$$

A few simulations (not presented in this paper) have been made with $\Delta x\omega_{pe}/c = 2$ or more. They all led to the growth of a numerical instability, with a wavelength of the order of a few grid cells only, and a slow but exponential growth. After a few hundred time steps, the increase of the total energy became unacceptable, and the divergence of the magnetic field was not negligible anymore. But simulations with a grid size $\omega_{pe}\Delta x/c = 0.5$ gave correct results.

As with the guiding centre code [10], there is no condition upon the grid size connected to the electron Larmor radius.

There are also a few restrictions on the magnetic field amplitude. The present algorithm implements the guiding centre theory of the electron motion. The guiding centre theory can be derived, as an asymptotic computation, as long as the electron gyrofrequency ω_{ce} is decoupled from other frequencies in the system [9]. Then, if $\omega_{ce} \sim \omega_{pe}$, the conditions for the asymptotic development are not met, and the guiding centre theory does not hold. Therefore, we must exclude the simulations where $\omega_{ce} \sim \omega_{pe}$. The guiding centre theory also requires that the magnetic field is not equal to zero. (This rather trivial requirement is redundant with the already mentioned prescription $\omega_{ce}\Delta t \gtrsim 1$.) The guiding centre approximation requires a smooth dependency of the electromagnetic field on the scale of the electron Larmor radius ρ_{Le}. This is not a problem, because the usual requirements for the discretization of the equations impose smooth variations on the scale of Δx, and with the guiding centre approximation $\Delta x > \rho_{Le}$.

Is any electron plasma β_e allowed? This parameter measures the ratio of the electron kinetic pressure to the magnetic pressure. The relation below shows this ratio, and the prescriptions (71) and (72) imply that it is majored by 1:

$$\beta_e = \left(\frac{v_{te}}{c}\right)^2 \left(\frac{\omega_{pe}}{\omega_{ce}}\right)^2 < 1. \tag{73}$$

When the simulation for a larger electron plasma beta is required, it is necessary to use an implicit code without the electron guiding centre approximation [8]. (Without the guiding centre approximation, there is no upper value for β_e, but the prescription for stability (71) is replaced by the accuracy requirement $\Delta t\omega_{ce} << 1$ discussed at the beginning of this section.)

The restriction on the ion plasma beta can be established on a similar ground

$$\beta_i < \frac{m_i}{m_e}. \tag{74}$$

This upper value is well above the values met in most magnetized space plasmas. (Having a high ion plasma beta and a low electron plasma beta implies that the ions have a much higher temperature than the electrons.)

To conclude this section, we should emphasise the fact that these conditions are necessary, but we have no proof that they are sufficient. We know that the implicit equations are unconditionally stable, if they are solved exactly. But the approximations made to solve them (linearization, predictor–corrector, etc.) may restrict the conditions of convergence. Cohen et al. [16] have studied various direct implicit schemes for the computation of the motion of the particles. The analysis is conducted for particles in particular electromagnetic fields conditions (harmonic oscillators with different strengths in the parallel and perpendicular direction), in order to address the questions of the stability, the accuracy, and unphysical acceleration rates (cooling and heating). The stability conditions mentioned in the present section are compatible with their conclusion, and Cohen et al. have shown that unphysical heating or cooling are proportional to Δt^3 for slow particles. Hewett and Langdon [8] in their paper on the direct implicit code with the electron full dynamics have addressed the question of stability when strong density inhomogeneities are met in the plasma. This question is not treated in the present paper. They have also studied the performance and accuracy of their algorithm in two particular test

cases (these cases correspond to a low magnetic field and cannot be reproduced in the context of the guiding centre approximation). It should be noted that very relevant studies have been conducted on the stability properties of the implicit moment method [3,5]; but their conclusions cannot be transposed crudely to the case of the direct implicit methods, even if some ideas might be developed in this context (that is out of the scope of the present paper).

5. Discussion and conclusion

This paper introduces a new algorithm for particle in cell collisionless plasma simulations that considers the guiding centre dynamics of the electrons and the full dynamics of the ions. Moreover, this code is implicit upon high frequency thermal fluctuations and allows for simulations with larger time steps than explicit PIC codes. Using a time step Δt greater than ω_{pe}^{-1} and ω_{pi}^{-1} is possible.

It was shown than we do not need to resolve the Debye length spatial scale. But, we must keep on the resolution of the electron inertial scale. In other words, $\lambda_D = v_{te}/\omega_{pe} < \Delta x < c/\omega_{pe}$.

The use of the electron guiding centre make this code interesting only for magnetized plasmas, and the constraints on the electron and ion plasma beta are given by (73) and (74). The constraint on the electron beta is rather strong, and make this code unable, for instance, to simulate all the collisionless magnetized space plasmas encountered in the solar system. But, most of the plasmas encountered in the Earth magnetosphere, for instance, have an electron $\beta_e < 1$, even when the ion plasma beta can reach large values. When the condition $\beta_e << 1$ is reached, this code allows for a quite significant increase of time step and simulation domain size compared to explicit PIC codes.

Because of the gain in time steps and grid size, it is less often necessary to use a reduced proton to electron mass ratio: sometimes, the real value can be introduced at almost the same cost, and allows for more direct comparisons between simulated and real plasmas.

It is, in the case of "rather cold electrons", possible to reach easily, even with an ordinary laptop computer, timescales and sizes that where beyond the scope of explicit particle simulations, such as the simulation of MHD waves over several periods.

We enter a domain of scales that is actually explored with hybrid codes.

We cannot describe all the thermal behavior of the electrons, but because of their finite mass, we can study their inertial effects (not possible for instance with the hybrid codes that use a fluid of massless electrons), and their acceleration (as they do not have to behave as a single fluid but kinetically).

As the displacement current is kept in the Ampère equation, the Poisson equation is still required, and charge density effects are taken into account. Therefore, this code allows for the simulation of electrostatic waves, as was shown in Section 3.3. This point is also an advantage over hybrid simulations.

The present code can also be compared with other kinetic plasma implicit codes.

The time decentering implicit code HIDENEK [1,2] exists in a version where electron guiding centres are taken into account. This versions allows for simulations with long time steps in magnetized plasmas. It is a first order code in Δt, while the present algorithm is supposed to be accurate up to the second order. The electron guiding centre motion is not treated with the same equations in Tanaka's algorithm. In particular, in Tanaka's code, the parallel and the perpendicular velocities are not derived at the same time, but at times $(n+\alpha)\Delta t$ and $(n+1/2)\Delta t$, where $\alpha \in [1/2, 1]$ is a time decentering parameter. In the present algorithm, the derivation of the electron motion is more accurate, and is based on simpler electron guiding centre equations of motion.

In the time decentering implicit time differencing for the Maxwell equations is applied to the Faraday and the Ampere equations. In the Ampere equation, the displacement current is time shifted with the electric current and the curl of the magnetic field. This allows, if required by a large grid cell, for implicitness over the inertial effects. Therefore, HIDENEK, even when used with electron guiding centres allows for simulations with $\Delta x > c/\omega_{pe}$. Therefore, it is not restricted to the simulation of low beta electrons.

Different versions of the moment method have been implemented in the codes VENUS [3] and CELESTE [4,5], up to now, for accurate simulations when $\omega_{ce}\Delta t < 1$. Actually, simulations with $\omega_{ce}\Delta t > 1$ are possible, and have been conducted where the $\mathbf{E} \times \mathbf{B}/B^2$ drift is taken into account.

The code developed by Hewett and Langdon [8] is also implicit upon the electron and ion plasma frequencies, but it describes the full dynamics of the electron. As said in the introduction, it is not well adapted to plasmas with a high magnetic field. I believe that the present algorithm and the direct implicit algorithm developed by Hewett and Langdon are rather complementary. The last one is more constrained on time step (because of the requirement $\Delta t\omega_{ce} < 1$), especially when the magnetic field is high, but allows for higher electron plasma betas β_e.

There remains a domain that is not yet accessible to implicit PIC plasma simulations: when the electron plasma frequency is of the same order as the electron cyclotron frequency. Nor the guiding centre implicit codes (not relevant when $\omega_{ce} \sim \omega_{pe}$), nor the implicit electron full dynamics codes (interesting when $\omega_{pe}\Delta t > 1$ but generally inaccurate when $\omega_{ce}\Delta t > 1$) can be used advantageously in this regime which remains a privileged domain for explicit PIC codes.

Acknowledgement

The author thanks J.C. Adam, A. Héron, and P. F. Lavallée for precious inputs and support.

Appendix A. Choice of a predictor of the electron velocities

At the stage of prediction, we must try to deduce how the system will evolve, but we have only an incomplete set of data (the set is completed at the stage of the correction). Therefore, we are in the domain of guesses rather than formal demonstration. This is a well-known weakness of the predictor–corrector algorithms and for this reason, different solutions for a predictor can be proposed. The choice between them is based on "general ideas" and experimentation. Three solutions are discussed here, and the last one is retained in the present paper.

The first, as in [7,8], consists of putting everything that is known at time n into the prediction:

$$\tilde{\mathbf{v}}_{n+1/2} = \mathbf{v}_{n-1/2} + \frac{\Delta t}{2}\bar{\mathbf{a}}_{n-1} - \frac{\mu\Delta t}{m}\nabla B_n + \frac{q\Delta t}{4m}\bar{\mathbf{v}}_{n-3/2} \times \mathbf{B}_n(\mathbf{x}_n) - \tilde{\mathbf{v}}_{n+1/2} \times \mathbf{\Theta}_n(\mathbf{x}_n), \tag{A.1}$$

the other terms are contained in the correction:

$$\delta\mathbf{v}_{n+1/2} = +\frac{q\Delta t}{2m}\mathbf{E}_{n+1} + \delta\mathbf{v}_{n+1/2} \times \mathbf{\Theta}. \tag{A.2}$$

Only one half of the magnitude of the electric acceleration ($\frac{\Delta t}{2}\bar{\mathbf{a}}_{n-1}$) is taken into account into the prediction, the other part ($\frac{q\Delta t}{2m}\mathbf{E}_{n+1}$) is in the correction. This solution has been tested. The predictor is good in the parallel direction, and bad in the perpendicular direction. Why? In the parallel direction, the guiding centres have typical velocities (v_{te}) that are an order of magnitude higher than the electric acceleration (because of the electron inertia). Therefore, taking only a half of the order of magnitude of the electric acceleration does not make a great difference. But in the perpendicular direction, the thermal motion is not contained in the guiding centre velocity (it is contained into the magnetic moment), and, to the first order, the amplitude of the velocity is the cross field drift, of amplitude $v_\perp \sim E/B$. Therefore, considering only a half of the electric field amplitude in the prediction causes a significant error, and the correction is of the same order of magnitude than the prediction. This does not fit the requirement that the correction should be much smaller than the prediction.

The second solution would consist of introducing the total order of magnitude of the electric acceleration into the prediction:

$$\tilde{\mathbf{v}}_{n+1/2} = \mathbf{v}_{n-1/2} + \Delta t\bar{\mathbf{a}}_{n-1} - \frac{\mu\Delta t}{m}\nabla B_n + \frac{q\Delta t}{4mc}\bar{\mathbf{v}}_{n-3/2} \times \mathbf{B}_n(\mathbf{x}_n) - \tilde{\mathbf{v}}_{n+1/2} \times \mathbf{\Theta}_n(\mathbf{x}_n) \tag{A.3}$$

and removing the added $\Delta t\bar{\mathbf{a}}_{n-1}/2$ from the correction,

$$\delta\mathbf{v}_{n+1/2} = +\frac{\Delta t}{2}\left(\frac{q}{m}\mathbf{E}_{n+1} - \bar{\mathbf{a}}_{n-1}\right) + \delta\mathbf{v}_{n+1/2} \times \mathbf{\Theta}. \tag{A.4}$$

This solution has been tested and gives indeed a good prediction of the perpendicular motion of the guiding centres. But the code does not work either, because of a bad behavior of the guiding centres in the parallel

direction. Taking only half of the order of magnitude of the parallel electric acceleration must be necessary to damp the high frequency ($\omega = \omega_{pe}$) plasma oscillations of the electrons.

The third solution, given in Section 2.3 by Eq. (28)–(30) is a compromise between the two above choices. It preserves the low pass filtering over the parallel electric field of the plasma oscillations, and give a correct estimate of the zeroth order $\mathbf{E} \times \mathbf{B}$ drift. It consists of a predictor that takes every thing known about the *parallel* acceleration into account (that is about half the total value), and the total order of magnitude of the *perpendicular* electric acceleration. This solution gives, as far as we could see, the best results; however, we have no formal proof that it is the optimal predictor–corrector scheme, and it is not certain that such a proof would exist for this choice and any other.

Appendix B. Demonstration of the Poisson correction formula

Let us take the divergence of (68):

$$\nabla \cdot (\mathbf{I} + \boldsymbol{\chi}_{\text{ion}} + \boldsymbol{\chi}) \cdot \mathbf{E} = \nabla \cdot \mathbf{Q}'$$

and the divergence of the Poisson corrected electric field,

$$\nabla \cdot \mathbf{E}_{n+1} = \nabla \cdot \mathbf{E} - \nabla^2 \Psi. = \rho_{n+1}.$$

When the electric field $\mathbf{E}$ and $\mathbf{E}_{n+1}$ are computed, the charge density ρ_{n+1} is not yet known, we know only its prediction $\tilde{\rho}_{n+1}$. Therefore, the Poisson equation is

$$\nabla^2 \Psi = \nabla \cdot \mathbf{Q}' - \nabla \cdot (\boldsymbol{\chi}_{\text{ion}} + \boldsymbol{\chi}) \cdot \mathbf{E} - \tilde{\rho}_{n+1} - \delta\rho_{n+1}, \tag{B.1}$$

where $\delta\rho_{n+1}$ still have to be expressed as a function of $\mathbf{E}_{n+1}$. The charge density (38) can be predicted as

$$\tilde{\rho}_{n+1} = +q_e \sum_{\text{GC}} S(\mathbf{X}_j - \tilde{\mathbf{x}}_{n+1}) + q_i \sum_{\text{ions}} S(\mathbf{X}_j - \mathbf{x}_{n+1}), \tag{B.2}$$

where $q_e = -1$ and $q_i = +1$ for a plasma of electrons and protons. The charge density correction is

$$\delta\rho_{n+1} = +q_e \sum_{\text{GC}} [S(\mathbf{X}_j - \mathbf{x}) - S(\mathbf{X}_j - \tilde{\mathbf{x}}_{n+1})], \tag{B.3}$$

where the sum is done only over the electron guiding centres. This field can be linearized trough the gradient of the shape factor, relative to the $\mathbf{X}_j$ components.

$$\delta\rho_{n+1} = +q_e \sum_{\text{GC}} -\nabla S(\mathbf{X}_j - \tilde{\mathbf{x}}_{n+1}) \delta\mathbf{x}_{n+1}.$$

Considering that only the charge density depends on the $\mathbf{X}_j$ components, this expression can be considered as the single divergence of the product of the shape factor and the displacement $\delta\mathbf{x}_{n+1}$. With (37), the charge density correction becomes

$$\delta\rho_{n+1} = -q_e \Delta t \sum_{\text{GC}} \nabla \cdot [S(\mathbf{X}_j - \tilde{\mathbf{x}}_{n+1}) \delta\mathbf{v}_{n+1/2}].$$

Comparing the above expression and $\delta\mathbf{J}_{n+1/2,\text{GC}} = \sum_{\text{GC}} + q_e \delta\mathbf{v}_{n+1/2} S(\mathbf{X}_j - \tilde{\mathbf{x}}_{n+1})$ we obtain a kind of correction of the charge conservation equation:

$$\delta\rho_{n+1} = -\Delta t \nabla \cdot \delta\mathbf{J}_{n+1/2,\text{GC}} \tag{B.4}$$

And using (57),

$$\delta\rho_{n+1} = -\nabla \cdot (\boldsymbol{\chi}_{\text{ion}} + \boldsymbol{\chi}) \cdot \mathbf{E}_{n+1} - \Delta t \nabla \cdot \mathbf{J}^*. \tag{B.5}$$

Let us reinject the above expression for $\delta\rho_{n+1}$ into Eq. (B.1). We find

$$\nabla^2 \Psi = \nabla \cdot (\mathbf{Q}' + \Delta t \mathbf{J}^*) - \nabla \cdot (\boldsymbol{\chi}_{\text{ion}} + \boldsymbol{\chi}) \cdot (\mathbf{E} - \mathbf{E}_{n+1}) - \tilde{\rho}_{n+1}. \tag{B.6}$$

As $\mathbf{E} - \mathbf{E}_{n+1} = \nabla\Psi$, we find Eq. (70).

Appendix C. Initialisation of Alfvén waves

The initialisation of the Alfvén waves in Section 3.1 is based on the bi-fluid theory of the cold plasma. The plasma consists of ions and electrons. The wave propagates along the magnetic field ($k = k_{\|}$). The dispersion equation of the waves is

$$\begin{aligned}&\omega^4 - s\omega^3(\omega_{ce} + \omega_{ci}) + \omega^2[\omega_{ce}\omega_{ci} - k^2c^2 - (\omega_{pe}^2 + \omega_{pi}^2)] + s\omega[(\omega_{ce} + \omega_{ci})k^2c^2 + \omega_{pe}^2\omega_{ci} + \omega_{pi}^2\omega_{ce}]\\ &\quad - k^2c^2\omega_{ce}\omega_{ci}\\ &\quad = 0.\end{aligned} \tag{C.1}$$

It has four roots. Among these roots, the two with the lowest frequency correspond to the right-hand side and left-hand side circularly polarized Alfvén waves. To initialize the simulations, this polynomial is solved numerically for a given wave vector k. Then, the chosen root is selected (depending on the choice of polarization). Then, a perturbation of the magnetic field is set:

$$B_y(x) = SB_1 \sin(kx), \tag{C.2}$$

$$B_z(x) = B_1 \cos(kx), \tag{C.3}$$

where $S = \pm 1$ depends on the polarization (right of left-hand side). The polarization of the electric field, and of the ion and electron velocities is set in accordance with the linearized cold plasma equations:

$$E_y(x) = \frac{\omega}{k}B_z(x) \quad \text{and} \quad E_z(x) = -\frac{\omega}{k}B_y(x), \tag{C.4}$$

$$V_{ey}(x) = Sc_{e1}B_y(x) \quad \text{and} \quad V_{ez}(x) = c_{e1}B_z(x), \tag{C.5}$$

$$V_{py}(x) = Sc_{p1}B_y(x) \quad \text{and} \quad V_{pz}(x) = c_{p1}B_z(x), \tag{C.6}$$

where $V_{ey}, V_{ez}, V_{py}, V_{pz}$ are the y and z components of the electron and ion velocity perturbations, and $c_{e1} = kS/(\omega + S\omega_{ce})\omega$ and $c_{p1} = -kSm_p/(\omega + S\omega_{ci})\omega m_e$.

References

[1] M. Tanaka, Macroscale implicit electromagnetic particle simulation of magnetized plasmas, Journal of Computational Physics 79 (1988) 209.

[2] M. Tanaka, S. Murakami, H. Takamaru, T. Sato, Macroscale Implicit Electromagnetic Particle Simulation of Inhomogeneous and Magnetized Plasmas in Multi-Dimensions, National Institute For Science, Nagoya, Japan, Research Report-1991.

[3] J.U. Brackbill, D.W. Forslund, An implicit method for electromagnetic plasma simulation in 2 dimensions, Journal of Computational Physics 46 (1982) 271–308.

[4] H.X. Vu, J.U. Brackbill, CELEST1D: an implicit, fully kinetic-model for low-frequency, electromagnetic plasma simulation, Computer Physics Communications 69 (1992) 253–276.

[5] P. Ricci, G. Lapenta, J.U. Brackbill, A simplified implicit Maxwell solver, Journal of Computational Physics 183 (2002) 117–141.

[6] G. Lapenta, J.U. Brackbill, P. Ricci, Kinetic approach to microscopic–macroscopic coupling in space and laboratory plasmas, Physics of Plasmas 13 (2006) 055904.

[7] B. Langdon, B. Cohen, A. Friedman, Direct implicit large time-step particle simulations of plasmas, Journal of Computational Physics 51 (1983) 107.

[8] D. Hewett, B. Langdon, Electromagnetic direct implicit plasma simulation, Journal of Computational Physics 72 (1987) 121.

[9] T. Northrop, The Adiabatic Motion of Charged Particles, Interscience Publishers, 1963.

[10] F. Mottez, J.C. Adam, A. Heron, A new guiding centre PIC scheme for electromagnetic higly magnetized plasma simulation, Computer Physics Communication 113 (1998) 1–22.

[11] C.K. Birsdall, B. Langdon, Plasma Physics via Computer Simulation, McGraw-Hill, New York, 1985.

[12] R.H. Hockney, J.W. Eastwood, Computer Simulations Using Particles, Adam Hilger, 1988.

[13] K. Rönnmark, Computation of the dielectric tensor of a Maxwellian plasma, Plasma Physics 25 (1983) 669.

[14] F. Mottez, G. Chanteur, A. Roux, Filamentation of plasma in the auroral region by an ion–ion instability: a process for the formation of bidimensional potential structures, Journal of Geophysical Research 97 (1992) 10801–10810.

[15] S.E. Parker, C.K. Birdsall, Numerical error in electron orbits with large $\omega_{ce}\Delta t$, Journal of Computational Physics 97 (1991) 91–102.

[16] B.I. Cohen, A.B. Langdon, A. Friedman, Implicit time integration for plasma simulation, Journal of Computational Physics 46 (1982) 15–38.